PHYSICAL REVIEW B **102**, 035125 (2020)

Editors' Suggestion

Eightfold fermionic excitation in a charge density wave compound

Xi Zhang,[1] Qiangqiang Gu,[1] Haigen Sun,[2] Tianchuang Luo,[1] Yanzhao Liu,[1] Yueyuan Chen,[1] Zhibin Shao,[3] Zongyuan Zhang,[2] Shaojian Li,[2] Yuanwei Sun,[1,4] Yuehui Li,[1,4] Xiaokang Li,[2,5] Shangjie Xue,[1,6] Jun Ge,[1] Ying Xing,[7] R. Comin,[6] Zengwei Zhu,[2,5] Peng Gao,[1,4,8] Binghai Yan,[9] Ji Feng,[1,10,*] Minghu Pan,[2,3,†] and Jian Wang[1,8,10,‡]

[1]*International Center for Quantum Materials, School of Physics, Peking University, Beijing 100871, China*
[2]*School of Physics, Huazhong University of Science and Technology, Wuhan 430074, China*
[3]*School of Physics and Information Technology, Shaanxi Normal University, Xi'an 710062, China*
[4]*Electron Microscopy Laboratory, School of Physics, Peking University, Beijing 100871, China*
[5]*Wuhan National High Magnetic Field Center, Huazhong University of Science and Technology, Wuhan 430074, China*
[6]*Department of Physics, Massachusetts Institute of Technology, Cambridge, Massachusetts 02139, USA*
[7]*Department of Materials Science and Engineering, School of New Energy and Materials,*
China University of Petroleum, Beijing 102249, China
[8]*Beijing Academy of Quantum Information Sciences, Beijing 100193, China*
[9]*Department of Condensed Matter Physics, Weizmann Institute of Science, Rehovot 7610001, Israel*
[10]*CAS Center for Excellence in Topological Quantum Computation, University of Chinese Academy of Sciences, Beijing 100190, China*

(Received 12 September 2019; accepted 24 June 2020; published 14 July 2020)

Unconventional quasiparticle excitations in condensed matter systems have become one of the most important research frontiers. Beyond twofold and fourfold degenerate Weyl and Dirac fermions, threefold, sixfold, and eightfold symmetry protected degeneracies have been predicted. However they remain challenging to realize in solid state materials. Here the charge density wave compound TaTe_4 is proposed to hold eightfold fermionic excitation and Dirac point in energy bands. High quality TaTe_4 single crystals are prepared, where the charge density wave is revealed by directly imaging the atomic structure and a pseudogap of about 45 meV on the surface. Shubnikov-de Haas oscillations of TaTe_4 are consistent with band structure calculation. Scanning tunneling microscopy/spectroscopy reveals atomic step edge states on the surface of TaTe_4. This work uncovers that the charge density wave is able to induce new topological phases and sheds new light on the novel excitations in condensed matter materials.

DOI: 10.1103/PhysRevB.102.035125

I. INTRODUCTION

Condensed matter systems, as a translational symmetry broken universe, host passionately pursued quasiparticle excitations analogous to high-energy elementary particles. A successful example is the prediction and observation of Dirac [1–3] and Weyl [4–6] fermions in solids protected by band topology. Weyl semimetals (WSMs) hold twofold degenerate Weyl points with nontrivial Chern number in energy bands. Fourfold degenerate Dirac points (DPs) with linear dispersion protected by time-reversal and inversion symmetry exist in Dirac semimetals (DSMs) and are stabilized by uniaxial rotation symmetries [7] or nonsymmorphic space group (SG) symmetries [1]. Recently, relations between Dirac or Weyl fermions and collective phenomena such as superconductivity (SC) is addressed [8–11], which is regarded as a route to realize topological SC and condensed matter analog of a third type of elementary particle, Majorana fermions [12].

However, the marvelous story is to be continued. First, classification of condensed matter fermionic excitations by Dirac, Weyl, and Majorana is incomplete. The 230 SG symmetries in three-dimensional (3D) lattices impose constraints weaker than Poincaré symmetry required in quantum field theory and therefore permit free fermionic excitations with no high-energy analog. Complete enumeration predicts threefold, sixfold, and eightfold degenerate fermions in condensed matter systems in addition to Dirac and Weyl fermions [13,14]. Threefold degeneracy has already been observed in MoP [15] and WC [16] while other types are still awaiting confirmation in real materials.

Second, apart from SC, another collective phenomenon of particular interest, the charge density wave (CDW), is much less studied in the context of topological materials. CDW is the ground state of a wide range of bulk compounds showing quasi-one-dimensional (quasi-1D) or quasi-two-dimensional (quasi-2D) lattice structures such as NbSe_3 [17], $(\mathrm{TaSe}_4)_2\mathrm{I}$ [18,19], and some transition metal dichalcogenides [20] arising from electron-phonon interaction. When cooling below Peierls transition temperature T_p, periodic modulation of charge density as well as structural distortion occur in these materials and an energy gap is opened at Fermi level. Similar to SC, CDW is also characterized by a complex order parameter $\Delta e^{i\varphi}$, where the phase φ is of fundamental importance, whose fluctuation forms a gapless current-carrying phase mode. However, the phase mode of the CDW can be pinned by

---

[*] Corresponding author: jfeng11@pku.edu.cn

[†] Corresponding author: minghupan@hust.edu.cn

[‡] Corresponding author: jianwangphysics@pku.edu.cn

impurities, lattice defects, and, in the commensurate case, the lattice itself. As a result, they can only give rise to nonlinear conductivity above a threshold electric field E_T [21].

Interplay between CDW and topology has been theoretically considered in the context of 2D DSMs [22], topological insulators (TIs) [23], topological WSMs [24,25], and DSMs [26]. In weak TI, the CDW is predicted to gap the surface states, however, create helical edge states on CDW domain walls [23]. In WSMs and DSMs, interaction effect may induce the CDW which gaps topologically protected degeneracy points and the phase of the CDW couples to the electromagnetic field in an analogous way to axion [25,26]. However, up to now, experimental studies of the CDW in topological semimetals are insufficient to test these hypotheses. Attempts of identifying topological phases in typical CDW compounds are also lacking.

In this article we report a topological semimetal phase in a CDW compound $TaTe_4$. $TaTe_4$ is structurally regarded as one of the simplest inorganic materials hosting a CDW [27]. Our calculation further points out that $TaTe_4$ is a topological semimetal both with and without the presence of the CDW. In its undistorted crystal structure $P4/mcc$ (SG124) without CDW, $TaTe_4$ holds DPs along high symmetry lines Γ-*Z* and *M*-*A*. A commensurate CDW phase in $TaTe_4$ is calculated to be the zero-temperature ground state and hold double Dirac point (DDP) with eightfold degeneracy at *A* as well as a Dirac point at *Z* in the CDW Brillouin zone. The calculated band structure of the CDW phase is consistent with the observed Shubnikov-de Haas (SdH) oscillations. The nontrivial topology of $TaTe_4$ is also suggested by the scanning tunneling spectroscopy (STS) detection of states residing on atomic step edges on the surface of $TaTe_4$. The coexistence of the CDW and fermionic excitations has been rarely reported before in other materials. Our results reveal the CDW-induced topological phases, which may lead to the possibility of dynamically tuning the topological properties of crystalline materials, and provide new insight into the interplay between the CDW and fermionic excitations.

II. EXPERIMENTAL AND CALCULATION METHODS

A. Band structure calculations

A density functional theory (DFT) calculation is performed using Vienna *ab initio* simulation package (VASP) [28] within the generalized gradient approximation, parametrized by Perdew, Burke, and Ernzerhof [29]. The energy cutoff for a plane-wave basis is set to 400 eV and the *k*-point mesh is taken as $11 \times 11 \times 11$ for the non-CDW phase and $5 \times 5 \times 5$ for the CDW phase. The CDW structure of $TaTe_4$ is obtained by fully relaxing a $2a \times 2b \times 3c$ supercell of the non-CDW phase of $TaTe_4$ after adding a random distortion. *a*, *b*, and *c* are lattice vectors in the non-CDW unit cell. The fully relaxation procedure was performed with a conjugated gradient algorithm, until the Hellmann-Feynman force on each atom is less than 10^{-3} eV/Å. The spin-orbit coupling effect is self-consistently included.

B. Single-crystal growth

High quality $TaTe_4$ single crystals are prepared by chemical vapor transport (CVT) technique in a multizone single crystal furnace [30]. Ta and Te powder are mixed at atomic ratio 1:4.3 and sealed with $5-10$ mg/cm^3 iodine in an evacuated quartz tube. The mixture is first heated to 1000 °C and kept for 12 h, and then slowly cooled down to room temperature. The quartz tube is then placed coaxially in the multizone furnace and the multizone function is used. The reaction zone is kept at 540 °C and growth zone at 440 °C for 7 days. After slowly cooling down to room temperature, bulk samples with metallic luster are obtained. Samples grown by this method are quite stable in atmosphere.

C. Sample characterization and transport measurements

Chemical composition of prepared crystals is confirmed by energy dispersive x-ray spectroscopy (EDS). The high-angle annular dark-field (HAADF) scanning transmission electron microscopy (STEM) image is performed on an aberration-corrected transmission electron microscope FEI Titan Cubed Themis G2 300. The single crystal property of the sample is confirmed by a Bruker D8 Advance powder x-ray diffractometer. $\rho - T$ measurement and magnetotransport measurement under magnetic field up to 15 T are performed in a Physical Property Measurement System (PPMS-16 T) by Quantum Design. Magnetoresistance up to 56 T is measured at Wuhan National High Magnetic Field Center with a pulsed magnetic field. Standard 4-probe/6-probe configuration is used throughout transport measurements.

D. Scanning tunneling microscopy (STM) measurements

For the STM study, the crystals chosen are approximately the size 2 mm × 1 mm×0.5 mm. Samples are first cleaved *in situ* at room temperature in an ultrahigh vacuum chamber with pressure lower than 1×10^{-10} Torr. After cleavage, the crystal exhibits a mirrorlike surface. An electrochemically etched tungsten wire is used as the STM tip. All measurements by STM were conducted at liquid helium temperature 4.2 K.

III. RESULTS AND DISCUSSION

A. Crystal structure and schematic electronic structure of $TaTe_4$

$TaTe_4$ crystallizes in a tetragonal $P4/mcc$ space group in the absence of the CDW. Quasi-1D chains along the *c* axis are formed by every Ta surrounded by 8 Te atoms [Fig. 1(a)] (also see Fig. S1 in the Supplemental Material (SM) [31]). At room temperature, $TaTe_4$ exhibits a commensurate CDW phase, which enlarges its unit cell to be $2a \times 2b \times 3c$ [Fig. 1(a)] (also see SM [31] Fig. S2). With CDW distortion, Ta atoms form Ta_3 clusters in the chain while Te atoms are slightly rotated around the Ta chains, which develop the equivalent 1D chains into three distinct types. The simulated CDW phase crystal structure is consistent with previous [38,39] and our experimental observations. The space group under the CDW phase is $P4/ncc$ where C_4 rotation and inversion symmetry are preserved. We prepare $TaTe_4$ single crystals using the CVT technique (details are presented in Methods section). The atomically resolved HAADF STEM image manifests the high quality of our sample [Fig. 2(a)]. Schematic structure clearly shows lattice distortions. After performing fast Fourier transform (FFT), four spots around the center are detected to

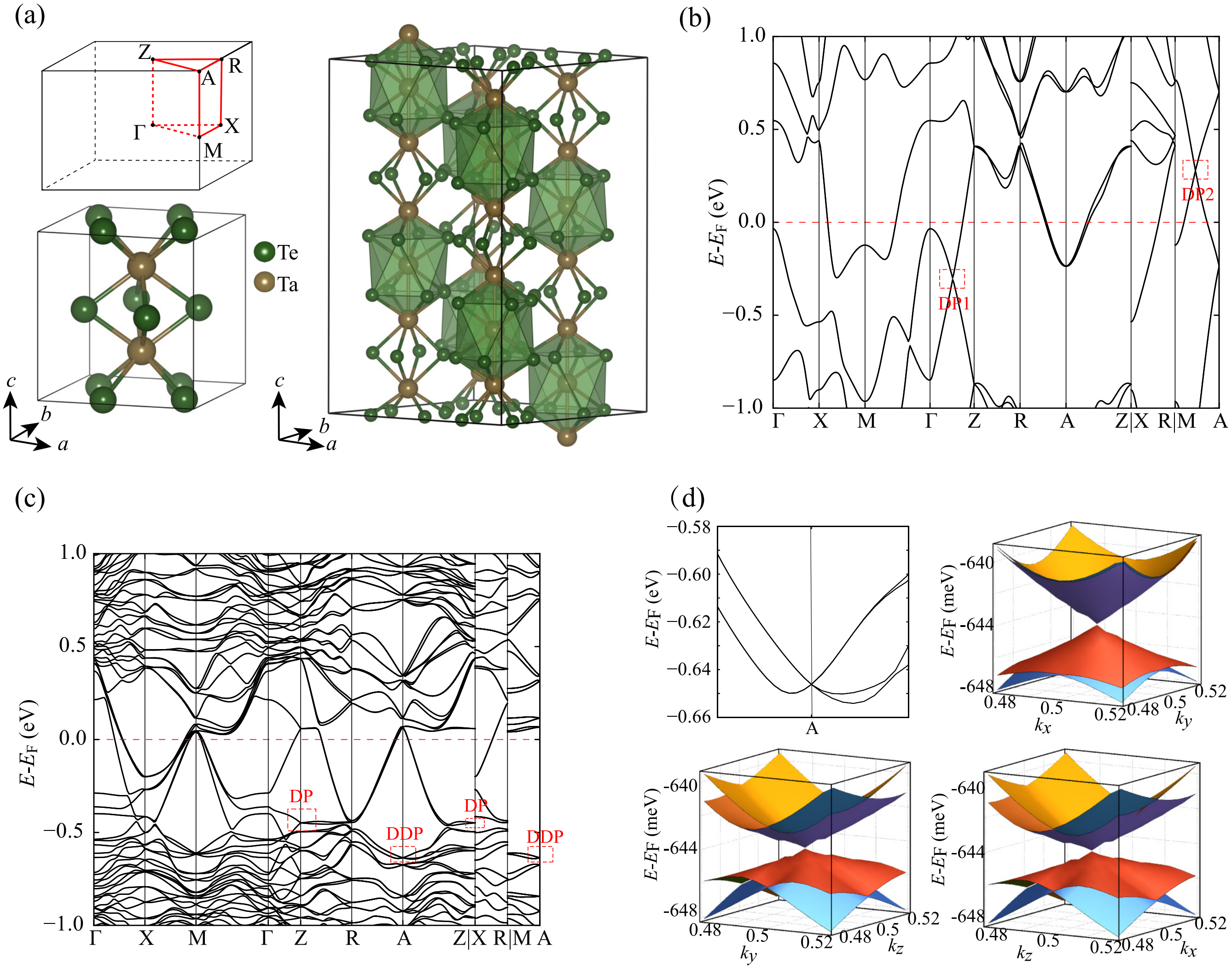

FIG. 1. Band structures of $TaTe_4$ with and without CDW. (a) Lower left panel and right panel show unit cell of non-CDW phase and CDW phase $TaTe_4$, where green polyhedrons indicate Ta_3 clusters. Upper left panel is the 3D bulk Brillouin zone of non-CDW/CDW phase $TaTe_4$ with high-symmetry points indicated. (b) Band structure along high-symmetry lines in the non-CDW Brillouin zone of $TaTe_4$ without CDW. Red dashed rectangles indicate DPs. (c) Band structure along high-symmetry lines in the CDW Brillouin zone of the CDW phase $TaTe_4$. Red dashed rectangles indicate DP and DDP. (d) Magnified dispersion around DDP in (c) and 3D linear dispersion around DDP. x, y, and z, respectively, correspond to the direction of a, b, and c axes.

represent an enlarged unit cell in the CDW phase (SM [31] Fig. S3(a)). XRD is also performed for the *ac* surface. Its result further confirms a uniform CDW phase in our sample (SM [31] Fig. S3(b)).

The band structure corresponding to the non-CDW structure of $TaTe_4$ is shown in Fig. 1(b). Two DPs are detected and marked by the red dashed rectangles in Fig. 1(b) near the Fermi level. The Dirac point DP1 lies in the Γ-*Z* line and 293 meV below the Fermi level, while the Dirac point DP2 lies 288 meV above the Fermi level in the *M*-*A* line. The Fermi energies of DPs (the energies of DPs relative to the Fermi level) in non-CDW $TaTe_4$ are comparable to that in Cd_3As_2 [40,41]. Figure 1(c) shows the band structure of $TaTe_4$ after considering CDW induced lattice distortion. The two DPs in the non-CDW band no longer exist. Instead, an eightfold degeneracy (or a DDP) at *A* point protected by symmetries of SG130 arises [13,14] at 644 meV below the Fermi level [Figs. 1(c) and 1(d)]. Also, a new Dirac point located 457 meV below the Fermi level appears at *Z* point [Fig. 1(c)]. As a result, the CDW dramatically modifies the band structure and Fermi surface (FS) of $TaTe_4$ and $TaTe_4$ holds eightfold fermionic excitation in the CDW phase. Our calculation results indicate that the CDW may strongly affect the topological property of a material, which has not been seriously considered before.

Interestingly, a surface CDW phase distinct from bulk CDW is observed by STM. At 4.2 K, a topographic image of the cleaved *ac* surface measured by STM shows a clear periodic modulation [bright strips in Fig. 2(c)]. FFT of an image shows the CDW peak at around $\pm 2\pi(\frac{1}{4a}, 0, \frac{1}{6c})$ (SM [31] Fig. S3(d)), indicating an enlarged $4a \times 6c$ surface unit cell which is larger than the bulk unit cell by the CDW lattice distortion ($2a \times 2b \times 3c$). Intriguingly, for the region where CDW modulation is present, a pseudogap of approximately

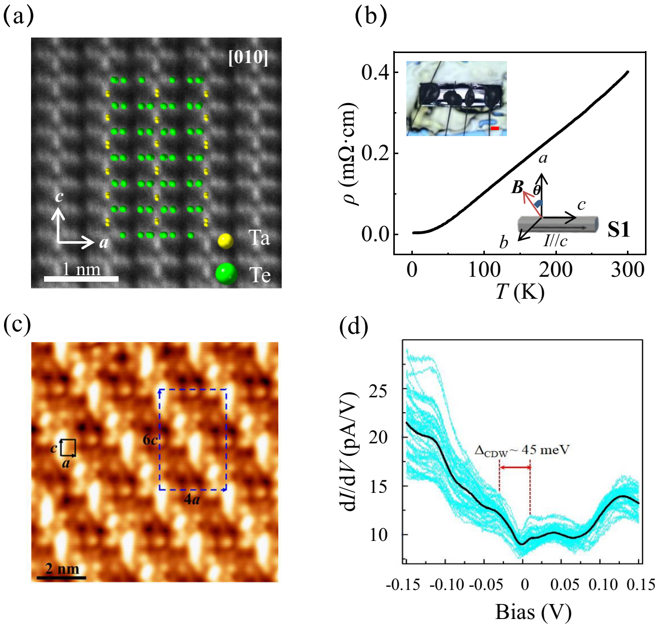

FIG. 2. Crystal structure, CDW, and ρ-T property of TaTe$_4$. (a) HAADF STEM image of TaTe$_4$ *ac* plane at room temperature with schematic structure. Scale bar represents 1 nm. (b) Sample resistivity as a function of temperature. Upper inset shows an optical image of one of our measured samples. Scale bar represents 200 μm. Lower inset is a schematic plot of magnetotransport measurement setup. (c) STM image of a cleaved *ac* surface with CDW modulation ($V_b = -250$ mV, $I_t = 250$pA, image size is 10×10 nm^2). Blue and black rectangles represent surface unit cell with and without CDW, respectively. (d) STS in a region with CDW modulation. Cyan curves are numerous dI/dV spectra measured at different locations on the bare surface areas (away from the defects) and the black curve is the averaged spectrum. A CDW gap of around 45 meV is clearly identified around Fermi level. Set point: $V_b = 150$ mV, $I_t = 200$ pA, the bias modulation for the lock-in technique is 9 mV.

45 meV is observed around Fermi level, as is shown in Fig. 2(d). This is interpreted as the CDW gap [42] since such a gap is reduced on the surface region where CDW modulation is less ordered (SM [31] Fig. S4).

B. Magnetoresistance and magnetic oscillations in TaTe$_4$

The resistivity-temperature (ρ-T) relation of TaTe$_4$ is shown in Fig. 2(b). Sample resistivity exhibits metallic behavior under zero magnetic field and saturates to around 3.5 $\mu\Omega$ cm below 10 K, with a rather large residual resistivity ratio (RRR $= \frac{\rho(300\text{ K})}{\rho(2\text{ K})}$) 111.

The magnetotransport measurement setup is schematically plotted in the lower inset of Fig. 2(b). Current is always along the *c* axis and the magnetic field is rotated relative to the sample in the *ab* plane. When magnetic field is applied along the *a* axis ($\theta = 0^\circ$), longitudinal magnetoresistance defined by MR $= \frac{\rho(B)-\rho(B=0)}{\rho(B=0)} \times 100\%$ saturates to around 3800% at 15 T [Fig. 3(a)] while pulsed magnetic field measurement up to 56 T reveals a more complicated structure of MR at higher fields [Figs. S5(a)–S5(c)]. When a magnetic field is applied along $\theta = 45^\circ$, MR does not fully saturate up to 15 T [Fig. 3(c)].

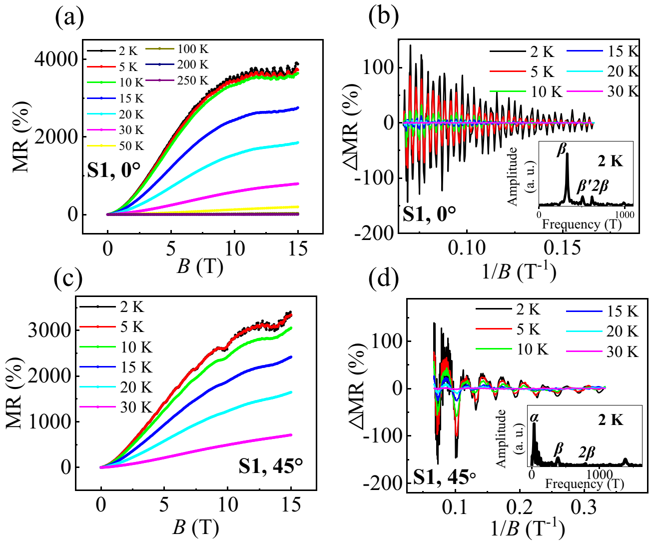

FIG. 3. Magnetoresistance and SdH oscillations in TaTe$_4$. (a) and (b) MR and SdH oscillations in TaTe$_4$ measured at $\theta = 0^\circ$. (a) MR as a function of magnetic field applied along *a* axis at various temperatures. (b) Oscillation components in (a) after subtracting a smooth background. Inset shows the FFT of oscillation at 2 K. (c) and (d) Results for $\theta = 45^\circ$.

At both magnetic field directions, oscillations of MR are clearly noticeable. By subtracting a smooth background, $1/B$ periodic SdH oscillation components are obtained [43,44], as are shown in Figs. 3(b) and 3(d). Oscillation frequencies can be obtained by performing FFT analysis of the data. The results for FFT of oscillations at lowest temperature are shown in the inset of Figs. 3(b) and 3(d), respectively. For $\theta = 0^\circ$, two oscillation frequencies, labeled by β and β', are observed, along with the second harmonic of β. We identify $F_\beta = 330$ T and $F_{\beta'} = 509$ T. They originate from equivalent pockets, as will be shown later. By Onsager relation [45] and assuming a spherical FS cross section, we obtain Fermi wave vector $k_F = 0.10$ Å^{-1} for β pocket. For $\theta = 45^\circ$, aside from frequency $F_\beta = 386$ T close to that observed for $\theta = 0^\circ$ and its harmonics, another smaller frequency $F_\alpha = 34$ T is observed. F_α corresponds to $k_F = 0.031$ Å^{-1}. As a result, the SdH oscillation pattern seems to be the superposition of two kinds of oscillations showing different frequencies. Additionally, a very high frequency (1383 T) is also detected. This kind of very high frequency oscillation is further revealed by ultrahigh magnetic field experiments (SM [31] Figs. S5(d)–S5(f)) which may originate from magnetic breakdown effect [46].

Often used for SdH oscillation analysis is a simplified version of the standard Lifshitz-Kosevich (LK) formula [45,47]:

$$\Delta\text{MR} \propto R_L R_D \cos\left[2\pi\left(\frac{F}{B}+\phi\right)\right], \tag{1}$$

where $R_L = \frac{\chi}{\sinh(\chi)}$, $\chi = \frac{2\pi^2 k_B m_c T}{e\hbar B}$ describes the damping of oscillation amplitude with temperature and $R_D = \exp(-\frac{\pi m_c}{eB\tau_Q})$ is the Dingle factor. m_c is the cyclotron mass and τ_Q is the quantum lifetime. An analysis of SdH oscillation patterns

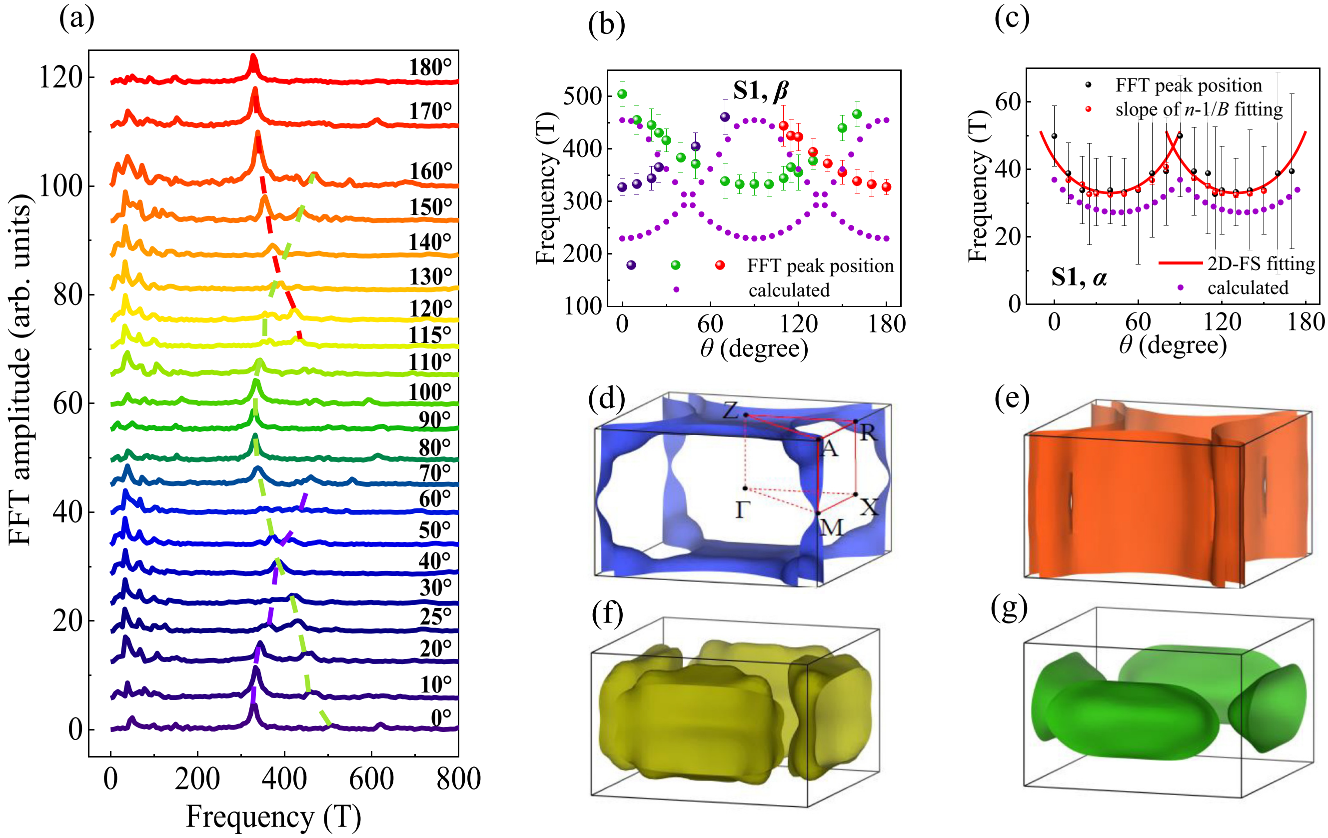

FIG. 4. Angular-dependent SdH oscillation and CDW phase Fermi surface of TaTe$_4$. (a) FFT of an oscillation component obtained by subtracting an eighth-order polynomial background at various θ. Dashed lines are guides to the eye. (b) Extracted high frequency peak positions in (a) as a function of θ. Colors of data indicate contributions from different but equivalent pockets. Violet points are numerical results from calculated FS in (g). (c) Extracted low frequency peak positions in (a) and frequencies extracted from Landau level fan diagrams as a function of θ. Violet points are numerical results from calculated FS in (d) and red lines are 2D-FS fitting to data. (d)–(g) The FS of bands 1–4 which crosses the Fermi level of the CDW phase TaTe$_4$ in the first Brillouin zone.

provides rich information on the electronic structure of TaTe$_4$ in the CDW phase, which tests the validity of our calculations. By fitting the oscillation amplitude as a function of temperature (SM [31] Fig. S7(a)), we obtain cyclotron mass $m_c = 0.33 m_e$ for β pocket at $\theta = 0°$, where m_e is the electron mass. Fermi velocity is also obtained as $v_F = 3.5 \times 10^5$ m/s. Further evidences [Fig. 4(b)] show that pocket β is of three-dimensional (3D) nature with rather low anisotropy. Thus, we can estimate the contribution to carrier concentration of a single β pocket by $n_\beta^{\text{pocket}} = \frac{2}{(2\pi)^3}\frac{4}{3}\pi k_F^3 = 3.4 \times 10^{19}\ \text{cm}^{-3}$, which is comparable with that obtained by Hall measurement at 2 K (SM [31] Fig. S8) $n^{\text{Hall}} = 1.34 \times 10^{20}\ \text{cm}^{-3}$. For α pocket at $\theta = 45°$, $m_c = 0.15\ m_e$ (SM [31] Fig. S7(b)) and $v_F = 2.32 \times 10^5$ m/s. Since α pocket is highly anisotropic [Fig. 4(c)], we cannot reasonably estimate its contribution to carrier concentration.

Angular-dependent magnetoresistance [48] or magnetic oscillation is a powerful tool to study FS anisotropy. An offset plot of FFT of oscillations at different θ (SM [31] Fig. S9) is shown in Fig. 4(a), where we can extract peak frequencies corresponding to α and β pockets. F_α is most prominent around $\theta = 45°$ and $\theta = 135°$ and can hardly be identified around $\theta = 0°$, 90°, and 180°, while F_β can be detected at all angles. Both F_α and F_β show repeated pattern every 90°, again consistent with the C_4 lattice symmetry. The experimentally detected frequencies can be identified by the extremal orbits in the calculated CDW phase FS, with calculated frequencies presented as violet points in Figs. 4(b) and 4(c). Four bands cross the Fermi level of TaTe$_4$ in CDW phase, among which bands 1 and 2 give rise to open FS while bands 3 and 4 exhibit closed Fermi pocket at the Fermi level, as is shown in Figs. 4(d)–4(g). Band 2 does not stably form a closed orbit and thus is hard to detect by magnetic oscillation. In comparison, although FS of band 1 is extended, it holds cylindrical sections along *Z*-*A* line, which may explain the quasi-2D behavior of F_α [red lines in Fig. 4(c)]. With these considerations, we assign F_α to band 1 and F_β to band 4 to obtain a best fit to our experimental data. The calculated effective mass m^* in this scenario is 0.21 m_e for F_β at 0° and 0.10 m_e for F_α at 45°, which is also in agreement with the cyclotron mass obtained by fitting the temperature dependence of oscillation amplitude [$m_c = 0.33\ m_e(\beta)$ and $0.15\ m_e(\alpha)$, respectively]. Therefore, the calculated band structure can explain the transport properties of the CDW phase TaTe$_4$ well, which validates our calculation. In addition, the non-CDW phase band structure cannot fit experimentally observed frequencies (SM [31]

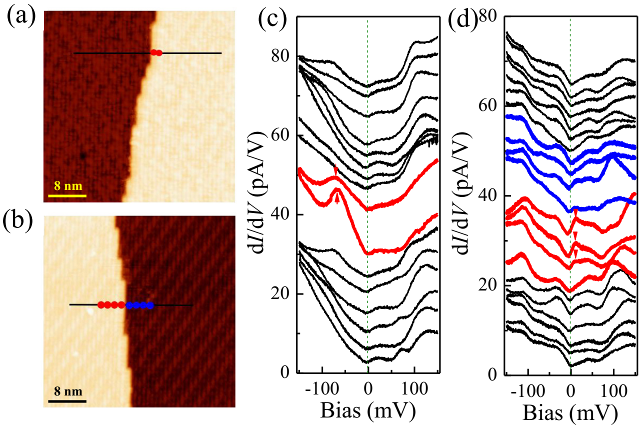

FIG. 5. States residing on step edges observed by STM. (a) STM image of an edge existing in a region with weak CDW modulation ($V_b = -70$ mV, $I_t = 200$ pA, image size is 40×40 nm^2). (b) STM image of an edge existing in a region with clear CDW modulation ($V_b = 12$ mV, $I_t = 200$ pA, image size is 40×40 nm^2). (c) Tunneling spectra at different locations along the line in (a). Spectra near the edge are shown in red. (d) Tunneling spectra at different locations along the line in (b). Spectra near the edge are shown in thick curves. Red arrows mark the appearance of edge states. All spectra were taken with the set point: $V_b = 150$ mV, $I_t = 200$ pA. The magnitude of the bias modulation for the lock-in technique is 9 mV.

Fig. S10), further confirming the CDW modulation on energy bands.

C. States residing on atomic step edges on the surface of TaTe$_4$

When a topological semimetal is reduced to two dimensions, 1D topological edge states could be detected. To further confirm the topological property of TaTe$_4$, we carry out STM measurement to study the edge of TaTe$_4$ terraces. The cleaved *ac* surfaces with steps of $2b$ ($b = a$ in TaTe$_4$) height are shown in Figs. 5(a) and 5(b). Such step edges can exist with weak [Fig. 5(a)] or clear [Fig. 5(b)] CDW modulation. Interestingly, edge states are detected under both circumstances at different biases. Figure 5(a) shows an edge existing in a region without clear CDW modulation, which is mostly parallel to Ta chain direction (*c* axis). We acquire tunneling differential conductance spectra, proportional to local density of states (LDOS), along a line across a step edge. Tunneling conductance has a finite value for all energies, further demonstrating the metallic properties revealed by transport measurement. On approaching the step edge, tunneling conductance shows a drastic increase at around −75 meV within the range of 2 nm [Fig. 5(c)], similar to that observed in WTe$_2$ [49]. Such an increase in LDOS is detected at several different edges at the same energy and thus cannot be well explained by a trivial edge state. In regions with clear CDW, an edge state appears at around 12 meV and coexists with the CDW gap [Fig. 5(d)]. The presence of the edge state makes the CDW gap seem to be narrower. These results show that TaTe$_4$ can hold edge states with or without clear CDW in the 2D limit, which not only suggests the topological nature of TaTe$_4$ but also points out that it is altered by the presence of the CDW.

IV. DISCUSSIONS

The CDW has been studied as a low dimensional phenomenon in various materials. Typically, it features a gap opened at Fermi level, which is identified as a transition behavior in ρ-T and insulating behavior below T_p, as in the case of (TaSe$_4$)$_2$I [18], K$_{0.3}$MoO$_3$ [50], and TaS$_3$ [51]. As for quasi-1D material NbSe$_3$, it remains metallic at low temperatures since one type of NbSe$_3$ chain remains metallic [17]. The above scenarios cannot be applied to TaTe$_4$, since CDW in TaTe$_4$ is commensurate and all chains exhibit trimerization with fixed relative phase [39]. According to our STS results, CDW does not fully gap the Fermi surface of TaTe$_4$, which indicates that under the CDW phase, 1D and 3D features exist simultaneously and only part of the electrons are involved in the CDW phase, as is also concluded by previous angle-resolved photoemission spectroscopy (ARPES) measurement [52]. The remaining DOS at Fermi level contributes to the sample conductance at low temperatures.

As a typical quasi-1D CDW compound, TaTe$_4$ is gifted to hold an exotic fermionic excitation as revealed by our DFT calculations. More interestingly, the fermionic excitations are altered by the CDW, which is not expected for typical quasi-1D compounds with the CDW transition whose FS is fully gapped by the CDW. The calculated eightfold degenerate point in TaTe$_4$ is closer to Fermi level than the triply degenerate point in MoP observed by ARPES [15], so that the related novel properties can be more easily detected. Direct observation of the DDP and DP in TaTe$_4$ by ARPES technique is highly desired. Our calculations also point out that Dirac line nodes [Fig. 1(d)], which may give rise to pairs of drumhead surface states [13], are associated with the DDP in TaTe$_4$. Dirac line nodes serve as a parent phase of all known topological semimetals. External symmetry-breaking perturbations, such as a magnetic field or uniaxial strain, may lead to DPs, Weyl points, or twofold degenerate line nodes [13]. Moreover, the existence of DP and DDP in TaTe$_4$ at different momenta may enable study of interplay between different kinds of fermions.

What is more interesting about TaTe$_4$ is that it also serves as a platform to study the interplay between CDW and fermionic excitations. Experimentally, the CDW has rarely been studied in the context of topological semimetals. In proposed Weyl semimetal candidate Y$_2$Ir$_2$O$_7$, the CDW was found to gap out the possible Weyl nodes [53]. The origin of the CDW in Y$_2$Ir$_2$O$_7$ is quite unusual and may be related to chiral symmetry breaking and axion dynamics. Theoretically, interaction between Weyl fermions at different momenta can induce the CDW, which gaps Weyl or Dirac points and the phase mode is predicted to present itself as the axion in condensed matter systems [25,26]. Considering the robustness of the CDW in TaTe$_4$, axion dynamics could be observed in TaTe$_4$ single crystal above the critical electrical field. Although the small resistance and the commensurate nature of the CDW hinder the investigation of the collective mode's contribution to the conductance of bulk TaTe$_4$, the nanoscale samples with higher resistance might offer the chance to detect axion dynamics and optical methods could also be helpful [21]. Another promising way is to investigate Nb doped TaTe$_4$, which is found to tune the CDW phase from commensurate to incommensurate [27,54]. Further investigations on the interplay between the CDW and topology in $\mathrm{TaTe_4}$ are of great research interest.

V. CONCLUSIONS

In summary, our results show that CDW phase $\mathrm{TaTe_4}$ is a topological semimetal with DDPs as well as DPs. The calculated band structure of $\mathrm{TaTe_4}$ is consistent with the observed SdH oscillations. STS detection of states residing on atomic step edges on the surface of $\mathrm{TaTe_4}$ further indicates the nontrivial topology of $\mathrm{TaTe_4}$. Therefore, our work suggests that $\mathrm{TaTe_4}$ is a promising platform to study physical phenomena related to CDW and free fermionic excitations in condensed matter systems.

ACKNOWLEDGMENTS

This work was financially supported by the National Key R&D Program of China (Grants No. 2018YFA0305600, No. 2017YFA0303302, and No. 2016YFA0301004), the National Natural Science Foundation of China (Grants No. 11888101, No. 11774008, No. 11574095, No. 91745115, No. 11725415, and No. 51672007), the Strategic Priority Research Program of Chinese Academy of Sciences (Grant No. XDB28000000), Beijing Natural Science Foundation (Z180010), and the Postdoctoral Innovative Talent Support Program of China (No. BX20200202). B.Y. acknowledges the financial support by the Willner Family Leadership Institute for the Weizmann Institute of Science, the Benoziyo Endowment Fund for the Advancement of Science, Ruth and Herman Albert Scholars Program for New Scientists. We gratefully acknowledge Gatan for the technique help. The authors acknowledge Electron Microscopy Laboratory in Peking University for the use of the Cs corrected electron microscope.

X.Z., Q.G., H.S., and T.L. contributed equally to this work.

[1] S. M. Young, S. Zaheer, J. C. Y. Teo, C. L. Kane, E. J. Mele, and A. M. Rappe, Phys. Rev. Lett. **108**, 140405 (2012).

[2] Z. Wang, Y. Sun, X.-Q. Chen, C. Franchini, G. Xu, H. Weng, X. Dai, and Z. Fang, Phys. Rev. B **85**, 195320 (2012).

[3] Z. K. Liu, B. Zhou, Y. Zhang, Z. J. Wang, H. M. Weng, D. Prabhakaran, S. K. Mo, Z. X. Shen, Z. Fang, X. Dai, Z. Hussain, and Y. L. Chen, Science **343**, 864 (2014).

[4] X. Wan, A. M. Turner, A. Vishwanath, and S. Y. Savrasov, Phys. Rev. B **83**, 205101 (2011).

[5] H. M. Weng, C. Fang, Z. Fang, B. A. Bernevig, and X. Dai, Phys. Rev. X **5**, 011029 (2015).

[6] S. Y. Xu, I. Belopolski, N. Alidoust, M. Neupane, G. Bian, C. L. Zhang, R. Sankar, G. Q. Chang, Z. J. Yuan, C. C. Lee, S. M. Huang, H. Zheng, J. Ma, D. S. Sanchez, B. K. Wang, A. Bansil, F. C. Chou, P. P. Shibayev, H. Lin, S. Jia, and M. Z. Hasan, Science **349**, 613 (2015).

[7] B. J. Yang and N. Nagaosa, Nat. Commun. **5**, 4898 (2014).

[8] H. Wang, H. Wang, H. Liu, H. Lu, W. Yang, S. Jia, X. J. Liu, X. C. Xie, J. Wei, and J. Wang, Nat. Mater. **15**, 38 (2016).

[9] H. Wang, H. C. Wang, Y. Q. Chen, J. W. Luo, Z. J. Yuan, J. Liu, Y. Wang, S. Jia, X. J. Liu, J. Wei, and J. Wang, Sci. Bull. **62**, 425 (2017).

[10] L. P. He, Y. T. Jia, S. J. Zhang, X. C. Hong, C. Q. Jin, and S. Y. Li, npj Quantum Mater. **1**, 16014 (2016).

[11] Y. Li, Q. Gu, C. Chen, J. Zhang, Q. Liu, X. Hu, J. Liu, Y. Liu, L. Ling, M. Tian, Y. Wang, N. Samarth, S. Li, T. Zhang, J. Feng, and J. Wang, Proc. Natl. Acad. Sci. USA **115**, 9503 (2018).

[12] M. Sato and Y. Ando, Rep. Prog. Phys. **80**, 076501 (2017).

[13] B. Bradlyn, J. Cano, Z. Wang, M. G. Vergniory, C. Felser, R. J. Cava, and B. A. Bernevig, Science **353**, aaf5037 (2016).

[14] B. J. Wieder, Y. Kim, A. M. Rappe, and C. L. Kane, Phys. Rev. Lett. **116**, 186402 (2016).

[15] B. Q. Lv, Z. L. Feng, Q. N. Xu, X. Gao, J. Z. Ma, L. Y. Kong, P. Richard, Y. B. Huang, V. N. Strocov, C. Fang, H. M. Weng, Y. G. Shi, T. Qian, and H. Ding, Nature (London) **546**, 627 (2017).

[16] J. Z. Ma, J. B. He, Y. F. Xu, B. Q. Lv, D. Chen, W. L. Zhu, S. Zhang, L. Y. Kong, X. Gao, L. Y. Rong, Y. B. Huang, P. Richard, C. Y. Xi, E. S. Choi, Y. Shao, Y. L. Wang, H. J. Gao, X. Dai, C. Fang, H. M. Weng, G. F. Chen, T. Qian, and H. Ding, Nat. Phys. **14**, 349 (2018).

[17] J. A. Wilson, Phys. Rev. B **19**, 6456 (1979).

[18] P. Gressier, A. Meerschaut, L. Guemas, J. Rouxel, and P. Monceau, J. Solid State Chem. **51**, 141 (1984).

[19] P. Gressier, M. H. Whangbo, A. Meerschaut, and J. Rouxel, Inorg. Chem. **23**, 1221 (1984).

[20] J. A. Wilson, F. J. Di Salvo, and S. Mahajan, Adv. Phys. **24**, 117 (1975).

[21] G. Gruner, Rev. Mod. Phys. **60**, 1129 (1988).

[22] L. Wang, H. Shi, S. Zhang, X. Wang, X. Dai, and X. C. Xie, arXiv:1012.5163.

[23] C. X. Liu, X. L. Qi, and S. C. Zhang, Physica E **44**, 906 (2012).

[24] H. Wei, S. P. Chao, and V. Aji, Phys. Rev. Lett. **109**, 196403 (2012).

[25] Z. Wang and S. C. Zhang, Phys. Rev. B **87**, 161107(R) (2013).

[26] R. X. Zhang, J. A. Hutasoit, Y. Sun, B. H. Yan, C. K. Xu, and C. X. Liu, Phys. Rev. B **93**, 041108(R) (2016).

[27] F. W. Boswell, A. Prodan, and J. K. Brandon, J. Phys. C: Solid State Phys. **16**, 1067 (1983).

[28] G. Kresse and J. Furthmuller, Phys. Rev. B **54**, 11169 (1996).

[29] J. P. Perdew, K. Burke, and M. Ernzerhof, Phys. Rev. Lett. **77**, 3865 (1996).

[30] F. Levy and H. Berger, J. Cryst. Growth **61**, 61 (1983).

[31] See Supplemental Material at http://link.aps.org/supplemental/10.1103/PhysRevB.102.035125 for additional data and analysis; also see Refs. [32–37] therein.

[32] K. Momma and F. Izumi, J. Appl. Crystallogr. **44**, 1272 (2011).

[33] M. N. Ali, L. M. Schoop, C. Garg, J. M. Lippmann, E. Lara, B. Lotsch, and S. S. Parkin, Sci. Adv. **2**, e1601742 (2016).

[34] J. P. Harrang, R. J. Higgins, R. K. Goodall, P. R. Jay, M. Laviron, and P. Delescluse, Phys. Rev. B **32**, 8126 (1985).

[35] L. P. He, X. C. Hong, J. K. Dong, J. Pan, Z. Zhang, J. Zhang, and S. Y. Li, Phys. Rev. Lett. **113**, 246402 (2014).

[36] Y. F. Zhao, H. W. Liu, C. L. Zhang, H. C. Wang, J. F. Wang, Z. Q. Lin, Y. Xing, H. Lu, J. Liu, Y. Wang, S. M. Brombosz, Z. L. Xiao, S. Jia, X. C. Xie, and J. Wang, Phys. Rev. X **5**, 031037 (2015).

[37] C. M. Wang, H. Z. Lu, and S. Q. Shen, Phys. Rev. Lett. **117**, 077201 (2016).

[38] K. D. Bronsema, S. Vansmaalen, J. L. Deboer, G. A. Wiegers, F. Jellinek, and J. Mahy, Acta Crystallogr. Sect. B **43**, 305 (1987).

[39] J. M. Corbett, L. G. Hiltz, F. W. Boswell, J. C. Bennett, and A. Prodan, Ultramicroscopy **26**, 43 (1988).

[40] S. Jeon, B. B. Zhou, A. Gyenis, B. E. Feldman, I. Kimchi, A. C. Potter, Q. D. Gibson, R. J. Cava, A. Vishwanath, and A. Yazdani, Nat. Mater. **13**, 851 (2014).

[41] T. Liang, Q. Gibson, M. N. Ali, M. Liu, R. J. Cava, and N. P. Ong, Nat. Mater. **14**, 280 (2015).

[42] P. Chen, W. W. Pai, Y. H. Chan, A. Takayama, C. Z. Xu, A. Karn, S. Hasegawa, M. Y. Chou, S. K. Mo, A. V. Fedorov, and T. C. Chiang, Nat. Commun. **8**, 516 (2017).

[43] Y. X. Gao, L. M. Xu, Y. Qiu, Z. M. Tian, S. L. Yuan, and J. F. Wang, J. Appl. Phys. **122**, 135101 (2017).

[44] X. Luo, F. C. Chen, Q. L. Pei, J. J. Gao, J. Yan, W. J. Lu, P. Tong, Y. Y. Han, W. H. Song, and Y. P. Sun, Appl. Phys. Lett. **110**, 092401 (2017).

[45] D. Shoenberg, *Magnetic Oscillations in Metals* (Cambridge University Press, Cambridge, 1984).

[46] S. Pezzini, M. R. van Delft, L. M. Schoop, B. V. Lotsch, A. Carrington, M. I. Katsnelson, N. E. Hussey, and S. Wiedmann, Nat. Phys. **14**, 178 (2018).

[47] D. X. Qu, Y. S. Hor, J. Xiong, R. J. Cava, and N. P. Ong, Science **329**, 821 (2010).

[48] X. Zhang, T. Luo, X. Hu, J. Guo, G. Lin, Y. Li, Y. Liu, X. Li, J. Ge, Y. Xing, Z. Zhu, P. Gao, L. Sun, and J. Wang, Chin. Phys. Lett. **36**, 057402 (2019).

[49] L. Peng, Y. Yuan, G. Li, X. Yang, J. J. Xian, C. J. Yi, Y. G. Shi, and Y. S. Fu, Nat. Commun. **8**, 659 (2017).

[50] X. M. Wang, L. Lu, H. M. Duan, B. J. Jin, and D. L. Zhang, Solid State Commun. **69**, 829 (1989).

[51] T. Sambongi, K. Tsutsumi, Y. Shiozaki, M. Yamamoto, K. Yamaya, and Y. Abe, Solid State Commun. **22**, 729 (1977).

[52] F. Zwick, H. Berger, M. Grioni, G. Margaritondo, L. Forro, J. LaVeigne, D. B. Tanner, and M. Onellion, Phys. Rev. B **59**, 7762 (1999).

[53] A. Juyal, A. Agarwal, and S. Mukhopadhyay, Phys. Rev. Lett. **120**, 096801 (2018).

[54] A. Prodan, V. Marinkovic, F. W. Boswell, J. C. Bennett, and M. Remskar, J. Alloy. Compd. **219**, 69 (1995).